PAPER

A Novel 3D Non-Stationary Vehicle-to-Vehicle Channel Model with Circular Arc Motions

Zixv SU[†], **Wei CHEN**[†], *and* **Yuanyuan YANG**[††a)], ***Nonmembers***

SUMMARY In this paper, a cluster-based three-dimensional (3D) non-stationary vehicle-to-vehicle (V2V) channel model with circular arc motions and antenna rotates is proposed. The channel model simulates the complex urban communication scenario where clusters move with arbitrary velocities and directions. A novel cluster evolution algorithm with time-array consistency is developed to capture the non-stationarity. For time evolution, the birth-and-death (BD) property of clusters including birth, death, and rebirth are taken into account. Additionally, a visibility region (VR) method is proposed for array evolution, which is verified to be applicable to circular motions. Based on the Taylor expansion formula, a detailed derivation of space-time correlation function (ST-CF) with circular arc motions is shown. Statistical properties including ST-CF, Doppler power spectrum density (PSD), quasi-stationary interval, instantaneous Doppler frequency, root mean square delay spread (RMS-DS), delay PSD, and angular PSD are derived and analyzed. According to the simulated results, the non-stationarity in time, space, delay, and angular domains is captured. The presented results show that motion modes including linear motions as well as circular motions, the dynamic property of the scattering environment, and the velocity of the vehicle all have significant impacts on the statistical properties.

key words: *vehicle-to-vehicle (V2V), cluster evolution algorithm, circular motions, non-stationarity*

1. Introduction

Nowadays, as an emerging future generation network, the sixth generation (6G) wireless communication network has received more and more attention [1]. The 6G technology aims to construct a stable space-air-ground-sea integrated network (SIGSIN), which is a solution to provide cost-effective and flexible wireless coverage [2]. As an indispensable research field of the SIGSIN, channel modeling deserves profound exploration. vehicle-to-vehicle (V2V) communication is regarded as an important communication scenario of channel modeling and naturally obtains a large amount of interest. In addition, as a key technology of 6G communication, the multi-input multi-output (MIMO) can deliver very high data rates and spectral efficiency [3]. It is logical to combine the MIMO with V2V communication system and the advantages of the combination include expanding communication applications and improving communication capability. In order to design and deploy a stable and efficient V2V communication system, the basic research on V2V channels becomes more and more important [4].

In order to build reasonable channel models, the characteristics of V2V channels should be fully taken into account. Firstly, low antenna heights cause a large number of effective local scatterers and the line-of-sight (LoS) component may be blocked easily [5]. Secondly, the transmitter (Tx) and the receiver (Rx) are mobile in V2V systems, which indicates the channel environment changes consistently and channel parameters are time-variant. Therefore, the channel non-stationarity is an essential feature for V2V channels.

At present, many researches have explored V2V communication channels in various scenarios. Generally, the research of V2V channels can be classified as channel measurements and channel modelings. It is well-known that actual V2V communication scenarios contain diversity as well as complexity and channel measurements have been carried out in different environments [6]–[13]. The measurement is presented in a typical underground garage entrance [6], it investigates the changing trend of the root mean square delay spread (RMS-DS) along the garage entrance and finds that the structure of the garage entrance has an influence on the RMS-DS. Two vehicles follow with each other in the mountain area and the measurement is conducted at center frequencies of 39 GHz and 2.4 GHz [7]. It found that the shadowing and fast fading at 2.4 GHz are more severe than those at 39 GHz. Based on channel measurements and analysis of V2V channel characteristics at 5.9 GHz in a tunnel scenario [8], it evaluates and compares the received power and RMS-DS outside and inside the tunnel. The non-stationarity for a highway scenario using the generalized local scattering function is accessed based on measurements [9]. It finds a strong correlation between the stationary time and the change of the distance. In addition, measurements are also conducted in the viaduct, tunnel, as well as cutting scenarios [11], and urban street scenarios [13].

In the meanwhile, channel modelings also undergo extensive and in-depth researches. Channel modelings can be subdivided into deterministic models [14]–[17] and stochastic models [18]–[25]. The establishment of deterministic models needs detailed measurement data and environmental parameters. Channel metrics derived from the ray-tracing simulation as well as from the measurement data are compared [14]. It shows measurement and simulation results of the received power show a very good agreement in the presence of the LoS component. The paper in [15] focuses on power delay profiles (PDPs) and channel gains in an ur-

Manuscript received November 10, 2023.
Manuscript revised February 22, 2024.
Manuscript publicized April 16, 2024.

[†]School of Automation, Wuhan University of Technology, Wuhan 430070, China.
[††]School of Information Engineering, Wuhan University of Technology, Wuhan 430070, China.
a) E-mail: yangyuanyuan@whut.edu.cn (Corresponding author)

DOI: 10.23919/transcom.2023EBP3178

Copyright © 2024 The Institute of Electronics, Information and Communication Engineers

ban four-way intersection scenario. The measurement data at 5.6 GHz in the city of Lund and the ray-tracing simulation result show a very good agreement. Undoubtedly, deterministic models have high correlation and consistency with the measurements and thus contain high accuracy. However, the structure of a detailed deterministic model has strict limitations on environmental parameters. A large number of computational time also increases the complexity.

On the contrary, stochastic models can be applicable to various scenarios and contain high computational efficiency. As a widely used method, geometry-based stochastic modelings (GBSMs) are extensively constructed to describe various channel environments. Furthermore, regular-shaped (RS) GBSM is regarded as a general modeling method. Macrocell V2V communication scenario is described by a cylinder around the Rx and the non-stationarity in time domain is verified [18]. A semicylinder model is constructed to model the tunnel scenario and the non-stationarity in time and space domain is validated [19]. However, due to the complexity and diversity of communication scenarios, a single geometric model is difficult to accurately characterize channels. Owing to the existence of local scatterers and far scatterers, it is prevailing to adopt combined geometrys [20]–[25]. Sphere models around the Tx and Rx are used to model local scatterers and multiple confocal elliptic-cylinder models represent the tapped delay line construction [20]. The impacts of vehicular traffic density on statistical properties and channel non-stationarity are investigated. A two-ring model is used to represent moving scatterers and multiple confocal ellipse models are used to represent the static scatterers in a two-dimensional urban communication scenario. The impact of different vehicular traffic densities is also investigated [21]. However, RS GBSMs still have certain limitations and the combination of several geometrys has certain difficulties in simulating complex channels accurately due to strict geometric constraints. Additionally, it also poses certain challenges in characterizing the non-stationarity in time, space, and frequency domains, as scatterers should not share a unitary velocity. Although a little complexity of irregular-shaped (IS) GBSMs [26]–[31], it can simulate the channel environment more accurately with increased clusters and provide different velocities of them. Dynamic clusters and static clusters are distinguished and high time-variance, non-stationarity, as well as vehicular traffic density of V2V channels are considered in [26]. To capture the non-stationarity, a time-array cluster evolution is developed. All clusters are randomly distributed with a uniform velocity and a Markov birth-and-death (BD) process is introduced to characterize the non-stationarity [27]. It shows a good agreement with measured results. Single and twin clusters are included to describe the channel environment and visibility region (VR) is to simulate the effect of the activity of clusters in [28]. The channel environment is modeled as randomly generated single clusters [29] and a time-array evolution algorithm is proposed. It shows the simulated properties can fit well the measurements. Clusters are divided into static/dynamic single/twin-clusters to capture the mixed-bouncing propagation. The impact of vehicular traffic density on channel statistics is investigated. The VR and BD process are integrated. The continuously arbitrary vehicular movement trajectory and soft cluster power handover are modeled. The generality of the proposed model is validated by comparing with measurements as well as ray-tracing (RT)-based results [30]. Substantially, in order to capture the non-stationarity, evolution algorithms are extensively used for IS GBSMs.

To sum up, IS GBSMs are more practical to describe complex channel environments accurately. Only limited scatterers are described around the Rx [18], and thus it contains a few strict application restrictions. Although far and local scatterers are taken into account to fully describe the channel environment, local scatterers are always around the Tx and Rx with fixed probability distributions and velocities [20], [24]. The non-stationarity is not considered in [21], [22]. Clusters with a uniform velocity cannot efficiently describe the stochastic channel. In addition, the direction of movement is assumed constant [26]–[29], and thus, it can only characterize channel properties with linear trajectories. Although the curved trajectory is described [30], array evolution is neglected and the derivation of time correlation with time-variation of angles is not fully demonstrated.

Actually, the curved motion of vehicles is prevalent for multiple scenarios. The turning at intersections, the movement of curved expressways on viaducts or highways, and the movement along the roundabout can be simultaneously considered as the circular arc motion of vehicles. As a prominent motion mode, channel characteristics of circular motion also deserve comprehensive and in-depth explorations. Additionally, the dynamic characteristic of scattering environments characterized by multiple moving clusters is a weighty part to affect the channel. However, not much literature emphasizes the research on the dynamic scattering environment. In order to fill up above gaps, the major contributions and novelties are summarized as follows.

1) A 3D non-stationary MIMO channel model with circular arc motions is proposed and the impact of antenna rotates is also incorporated. Clusters are given different velocities and directions in order to characterize complex urban communication scenarios.

2) A novel time-array evolution algorithm with time-array consistency is proposed. For time evolution, in addition to the death of survival clusters and the birth of new clusters, the rebirth of dead clusters is also taken into account. For array evolution, a VR method is developed, which is verified to be applicable to the circular arc motion.

3) By applying the Taylor expansion formula, the detailed derivation of space-time correlation function (ST-CF) is shown. In addition, Doppler power spectrum density (PSD), quasi-stationary interval, instantaneous Doppler frequency, RMS-DS, delay PSD, and angular PSD are derived and investigated. The channel characteristics with linear motion and circular motion as well as the channel characteristics in low dynamic scattering environment and in low dynamic scattering environment are compared and analyzed.

The remainder of this article is structured as follows.

Section 2 describes the 3D cluster-based channel model, in which time-variant channel parameters are derived. Cluster evolution algorithm with time-array consistency is developed in Sect. 3. Statistical properties including ST-CF, Doppler PSD, quasi-stationary interval, instantaneous Doppler frequency, RMS-DS, delay PSD, and angular PSD are derived in Sect. 4. Numerical results are simulated and analyzed in Sect. 5. Finally, conclusion is drawn in Sect. 6.

2. 3D Non-Stationary V2V Channel Model

2.1 Description of the Proposed Channel Model

In this section, we propose a non-stationary V2V communication GBSM. It is well known that the motion mode of the vehicle is influenced by the velocity and the direction. A typical actual scenario of circular arc motion is shown in Fig. 1. The Tx and Rx move along the curved roads in opposite directions. Scattering components may be generated by moving vehicles, pedestrians, and buildings on both sides of the road. The channel model is established in the global coordinate system (GCS) as shown in Fig. 2. The velocity of the Tx and Rx are V_{T} and V_{R}, respectively. The azimuth angle of the velocity of the Tx and Rx are θ_{T} and θ_{R}, respectively.

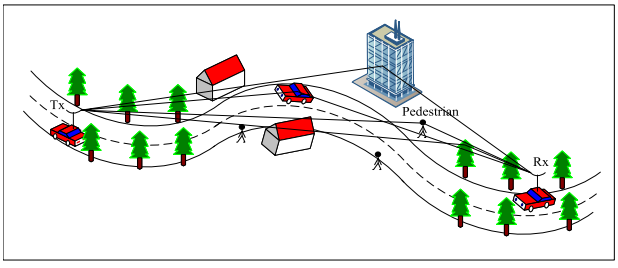

Fig. 1 Typical scenario of circular arc motions.

The elevation angle relative to xy plane and azimuth angle in the xy plane of the antenna array of the Tx are α_{T} and β_{T}, respectively. Analogously, the elevation angle and azimuth angle of the recieving antenna array are α_{R} and β_{R}, respectively. The angular velocity of the Tx and Rx are defined as ω_1 and ω_2. Considering that sufficent scatterers exist in complex urban areas, multi-bounced (MB) components are regarded as domainating multipath components (MPCs). Twin clusters are used to represent MB components. $C_{\mathrm{n}}^{\mathrm{T}}$ and $C_{\mathrm{n}}^{\mathrm{R}}$ are defined as the fisrt and the last cluster of the n-th MB component, which are generated around the Tx and Rx, respectively. The number of rays is randomly generated within clusters obeying Possion distribution. The m-th ray of $C_{\mathrm{n}}^{\mathrm{T}}$ and $C_{\mathrm{n}}^{\mathrm{R}}$ can be defined as $C_{\mathrm{n,m_n}}^{\mathrm{T}}$ and $C_{\mathrm{n,m_n}}^{\mathrm{R}}$, respectively. The velocity of $C_{\mathrm{n}}^{\mathrm{T}}$ and $C_{\mathrm{n}}^{\mathrm{R}}$ are $V_{\mathrm{n}}^{\mathrm{T}}$ and $V_{\mathrm{n}}^{\mathrm{R}}$, respectively. The moving direction of each cluster is assumed linear, and the n-th twin cluster moves with angle $\theta_{\mathrm{n}}^{\mathrm{T}}$ and $\theta_{\mathrm{n}}^{\mathrm{R}}$. The initial horizontal distance between the Tx and the Rx is D. The azimuth angle of department (AAoD) of the LoS component can be written as $\omega_{\mathrm{LoS}}(t)$. The elevation angle of department (EAoD) and AAoD of the MB component via $C_{\mathrm{n,m_n}}^{\mathrm{T}}$ can be written as $\omega_{\mathrm{n,m_n}}^{\mathrm{T}}(t)$ and $\gamma_{\mathrm{n,m_n}}^{\mathrm{T}}(t)$. The elevation angle of arrival (EAoA) and the azimuth angle of arrival (AAoA) implinging on $C_{\mathrm{n,m_n}}^{\mathrm{T}}$ can be written as $\omega_{\mathrm{n,m_n}}^{\mathrm{R}}(t)$ and $\gamma_{\mathrm{n,m_n}}^{\mathrm{R}}(t)$. The MIMO arrays can be described as a matrix of dimension $M_{\mathrm{T}} \times M_{\mathrm{R}}$ to reflect channel propagation properties, which is defined as $H(t) = [h_{\mathrm{ij}}(t)]_{M_{\mathrm{T}} \times M_{\mathrm{R}}}$. The spacing between two adjacent antennas of the Tx and Rx are δ_{T} and δ_{R}, respectively. We define $k_{\mathrm{p}} = \frac{M_{\mathrm{T}}-2p+1}{2}$ and $k_{\mathrm{q}} = \frac{M_{\mathrm{R}}-2q+1}{2}$ as the p-th antenna of the transmitting array and the q-th antenna of the receiving array.

2.2 Local Coordinate System

It is difficult to calculate channel parameters relative to the

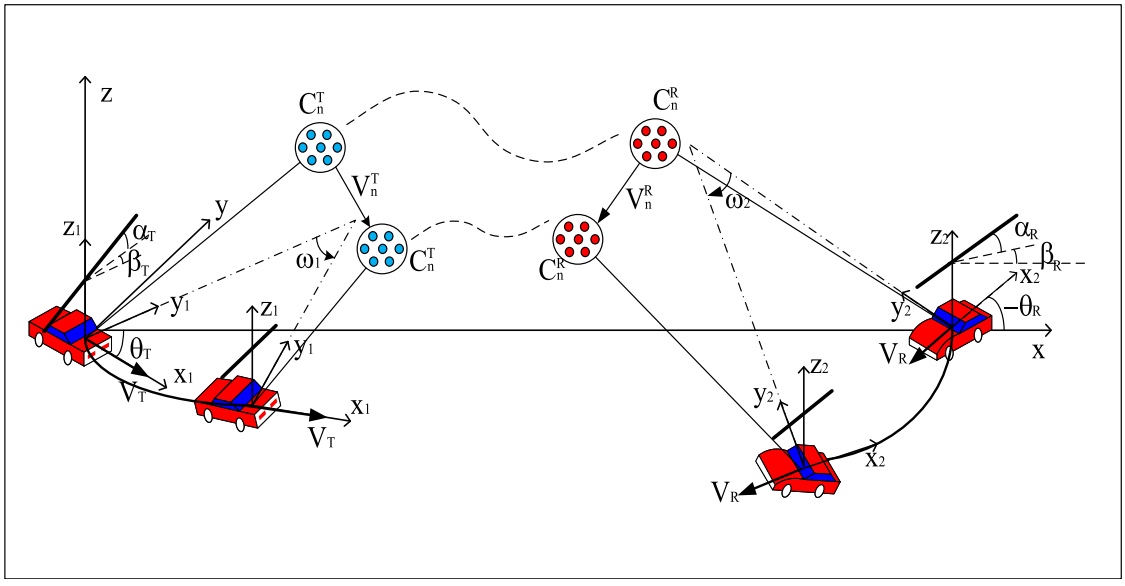

Fig. 2 V2V communication scenario with circular arc motions.

Tx and Rx in the GCS, due to nonlinear motions. At this point, local coordinate systems (LCS) are introduced for the transceivers. For the vehicle moving in a circle, the speed vector is always perpendicular to the line from the vehicle to the circle center. Therefore, the x_1 axis is consistent with the velocity direction, while the y_1 axis points towards the circle center in the LCS $x_1y_1z_1$ of the Tx. Due to the two-dimensional motion in the xy plane, in principle, LCSs are products of the GCS rotating around the z-axis and translating in the xy plane. Corrspondingly, the x_2 axis is opposite to the velocity direction, while the y_2 axis points towards the circle center in the LCS $x_2y_2z_2$ of the Rx. At the initial time, the speed vector is $\vec{V}_{\mathrm{T/R}}(0) = ||V_{\mathrm{T/R}}||(\cos\theta_{\mathrm{T/R}}, \sin\theta_{\mathrm{T/R}}, 0)^{\mathrm{T}}$. To convert the GCS xyz to the LCS $x_{1/2}y_{1/2}z_{1/2}$, the ratation matrix R_{GL} is calculated as

$$R_{\mathrm{GL}}^{\mathrm{T/R}} = \begin{pmatrix} \cos\theta_{\mathrm{T/R}} & -\sin\theta_{\mathrm{T/R}} & 0 \\ \sin\theta_{\mathrm{T/R}} & \cos\theta_{\mathrm{T/R}} & 0 \\ 0 & 0 & 1 \end{pmatrix} \tag{1}$$

In the LCS, the velocity vector is $\vec{V}_{\mathrm{T/R}}^{\mathrm{LCS}}(t) = ||V_{\mathrm{T/R}}||(\cos\omega_{1/2}t, \sin\omega_{1/2}t, 0)^{\mathrm{T}}$. Therefore the time-variant speed vector $\vec{V}_{\mathrm{T/R}}(t)$ can be calculated as

$$\begin{aligned} \vec{V_{\mathrm{T/R}}}(t) &= R_{\mathrm{GL}}^{\mathrm{T/R}}\vec{v}_{\mathrm{T}}^{\mathrm{LCS}}(t) = \begin{pmatrix} V_{\mathrm{xT}}(t) \\ V_{\mathrm{yT}}(t) \\ V_{\mathrm{zT}}(t) \end{pmatrix} \\ &= ||V_{\mathrm{T/R}}|| \begin{pmatrix} \cos(\omega_{1/2}t + \theta_{\mathrm{T/R}}) \\ \sin(\omega_{1/2}t + \theta_{\mathrm{T/R}}) \end{pmatrix} \end{aligned} \tag{2}$$

The Tx/Rx moves at angular velocity $\omega_{1/2}$ and the LCS always rotates with changes in speed vector. Thus, the time-variant LCS $x_{1/2}y_{1/2}z_{1/2}$ is derived according to the rotation matrix $R_{\mathrm{LCS1/LCS2}}$ as follows.

$$R_{\mathrm{LCS1/LCS2}}(t) = \begin{pmatrix} \cos\omega_{1/2}t & -\sin\omega_{1/2}t & 0 \\ \sin\omega_{1/2}t & \cos\omega_{1/2}t & 0 \\ 0 & 0 & 1 \end{pmatrix} \tag{3}$$

Linear antenna arrays (ULA) always maintain a fixed angle with the direction of the movement and thus, the orientation of the antennas is also time-varying in the GCS. The initial ULA vector is calculated as $\vec{A}_{\mathrm{p/q}}^{\mathrm{T/R}}(0) = k_{\mathrm{p/q}}\delta_{\mathrm{T/R}}(\cos\alpha_{\mathrm{T/R}}\cos\beta_{\mathrm{T/R}}, \cos\alpha_{\mathrm{T/R}}\sin\beta_{\mathrm{T}}, \sin\alpha_{\mathrm{T}})^{\mathrm{T}}$. The time-variant transmitting ULA vector can be computed as

$$\begin{aligned} \vec{A}_{\mathrm{p/q}}^{\mathrm{T/R}}(t) &= (R_{\mathrm{GL}}^{\mathrm{T/R}})^{-1}R_{\mathrm{LCS1/LCS2}}(t)R_{\mathrm{GL}}^{\mathrm{T/R}}\vec{A}_{\mathrm{p/q}}^{\mathrm{T/R}}(0) \\ &= k_{\mathrm{p/q}}\delta_{\mathrm{T/R}} \begin{pmatrix} \cos(\omega_{1/2}t + \beta_{\mathrm{T/R}})\cos\alpha_{\mathrm{T/R}} \\ \sin(\omega_{1/2}t + \beta_{\mathrm{T/R}})\cos\alpha_{\mathrm{T/R}} \\ \sin\alpha_{\mathrm{T/R}} \end{pmatrix} \end{aligned} \tag{4}$$

2.3 Channel Impulse Response

MPCs consist of the LoS component and MB components. Therefore, the channel impulse response (CIR) is expressed as

$$\begin{aligned} h_{\mathrm{pq}}(t,\tau) = &\sqrt{\tfrac{K}{K+1}}h_{\mathrm{pq}}^{\mathrm{LoS}}(t)\delta(\tau - \tau_{\mathrm{LoS}}(t)) \\ &+\sqrt{\tfrac{1}{K+1}}\textstyle\sum_{n=1}^{N}\sqrt{P_{\mathrm{n}}(t)}h_{\mathrm{pq}}^{\mathrm{n}}(t)\delta(\tau - \tau_{\mathrm{n}}(t)) \end{aligned} \tag{5}$$

where

$$\begin{aligned} h_{\mathrm{pq}}^{\mathrm{LoS}}(t) = &\ e^{j2\pi\int_0^t f_{\mathrm{LoS}}^{\mathrm{T}}(t')+f_{\mathrm{LoS}}^{\mathrm{R}}(t')dt'} \\ &e^{j\frac{2\pi}{\lambda}(A_{\mathrm{p}}^{\mathrm{T}}(t)s_{\mathrm{LoS}}^{T}(t)+A_{\mathrm{q}}^{\mathrm{R}}(t)s_{\mathrm{LoS}}^{R}(t))} \end{aligned} \tag{6}$$

$$\begin{aligned} h_{\mathrm{pq}}^{\mathrm{n}}(t) = &\ e^{j2\pi\int_0^t f_{\mathrm{n},\mathrm{m_n}}^{\mathrm{T}}(t')+f_{\mathrm{n},\mathrm{m_n}}^{\mathrm{R}}(t')dt'} \\ &e^{j\frac{2\pi}{\lambda}(A_{\mathrm{p}}^{\mathrm{T}}(t)s_{\mathrm{n},\mathrm{m_n}}^{T}(t)+A_{\mathrm{q}}^{\mathrm{R}}(t)s_{\mathrm{n},\mathrm{m_n}}^{R}(t))} \end{aligned} \tag{7}$$

where K and $P_{\mathrm{n}}(t)$ denote the Rician factor and the normalized power of the n-th MB component, respectively. $N(t)$ and λ denote the sum of clusters and the carrier wavelength, respectively. The delay of the LoS component is $\tau_{\mathrm{LoS}}(t)$. Delays of rays within the clusters are assumed indistinguishable, which are equivalent to the delay via the n-th twin-cluster, $\tau_{\mathrm{n}}(t)$. $f_{\mathrm{LoS}}^{\mathrm{T}}(t)$ and $f_{\mathrm{LoS}}^{\mathrm{R}}(t)$ are time-variant Doppler frequency of the LoS component of the Tx and Rx, repsectively. $f_{\mathrm{n},\mathrm{m_n}}^{\mathrm{T/R}}(t')$ denotes the Doppler frequency of the Tx/Rx and $C_{\mathrm{n}}^{\mathrm{T/R}}$ of the n-th MB component. $s_{\mathrm{n},\mathrm{m_n}}^{\mathrm{T}}(t)$ and $s_{\mathrm{n},\mathrm{m_n}}^{\mathrm{R}}(t)$ are the unit vector of the angle of departure (AoD) and the unit vector of the angle of arrival (AoA), i.e., $s_{\mathrm{n},\mathrm{m_n}}^{\mathrm{T/R}}(t) = (\cos\gamma_{\mathrm{n},\mathrm{m_n}}^{\mathrm{T/R}}(t)\cos\omega_{\mathrm{n},\mathrm{m_n}}^{\mathrm{T/R}}(t), \cos\gamma_{\mathrm{n},\mathrm{m_n}}^{\mathrm{T/R}}(t)\sin\omega_{\mathrm{n},\mathrm{m_n}}^{\mathrm{T/R}}(t), \sin\gamma_{\mathrm{n},\mathrm{m_n}}^{\mathrm{T/R}}(t))$.

2.4 Time-Variant Parameters

In the GCS, the location vector of the Tx $\vec{L}_T(t) = (L_{\mathrm{xT}}(t), L_{\mathrm{yT}}(t), L_{\mathrm{zT}}(t))^{\mathrm{T}}$ is computed as $\vec{L}_T(t) = \vec{L}_T(0) + \int_0^t \vec{V}_{\mathrm{T}}(t')dt' = \frac{||v_{\mathrm{T}}||}{\omega_1}(\sin(\theta_{\mathrm{T}} + \omega_1 t) - \sin\theta_{\mathrm{T}}, \cos\theta_{\mathrm{T}} - \cos(\theta_{\mathrm{T}} + \omega_1 t), 0)^{\mathrm{T}}$. Similarly, $\vec{L}_R(t) = (L_{\mathrm{xR}}(t), L_{\mathrm{yR}}(t), L_{\mathrm{zR}}(t))^{\mathrm{T}} = \frac{||v_{\mathrm{R}}||}{\omega_2}(D + \sin(\theta_{\mathrm{R}} + \omega_2 t) - \sin\theta_{\mathrm{R}}, \cos\theta_{\mathrm{R}} - \cos(\theta_{\mathrm{R}} + \omega_2 t), 0)^{\mathrm{T}}$.

The speed vector of the n-th cluster around the Tx/Rx is expressed as $\vec{V}_{\mathrm{n}}^{\mathrm{T/R}} = (V_{\mathrm{n}}^{\mathrm{xT/xR}}, V_{\mathrm{n}}^{\mathrm{yT/yR}}, V_{\mathrm{n}}^{\mathrm{zT/zR}})^{\mathrm{T}}$. Twin clusters are formed by the combination of two single clusters. Single clusters are randomly distributed around the Tx and Rx. The generation of single clusters is dependent on the distance from the n-th twin-cluster to the Tx/Rx $D_{\mathrm{n}}^{\mathrm{T/R}}(t)$ as well as the AoD/AoA. At the initial time, considering that angular variations for each ray are distinguishable, the AAoD/AAoA and EAoD/EAoA of the m-th ray within the n-th twin-cluster can be calculated as follows. In addition, the probability distribution for partial channel parameters is organized in Table 1.

$$\omega_{\mathrm{n},\mathrm{m_n}}^{\mathrm{T/R}}(t) = \omega_{\mathrm{n}}^{\mathrm{T/R}}(t) + \Delta\omega_{\mathrm{n},\mathrm{m_n}}^{\mathrm{T/R}} \tag{8}$$

$$\gamma_{\mathrm{n},\mathrm{m_n}}^{\mathrm{T/R}}(t) = \gamma_{\mathrm{n}}^{\mathrm{T/R}}(t) + \Delta\gamma_{\mathrm{n},\mathrm{m_n}}^{\mathrm{T/R}} \tag{9}$$

where $\omega_{\mathrm{n}}^{\mathrm{T/R}}(t)$ and $\omega_{\mathrm{n}}^{\mathrm{T/R}}(t)$ are the AAoD/AAoA and EAoD/EAoA of the n-th twin cluster. $\Delta\omega_{\mathrm{n},\mathrm{m_n}}^{\mathrm{T/R}}$ and $\Delta\gamma_{\mathrm{n},\mathrm{m_n}}^{\mathrm{T/R}}$ are offset angles.

The location vector of the m-th ray within n-th cluster

Table 1 Distribution of relevant channel parameters.

Parameter	Distribution	Mean	Derivation
$\omega_{\mathrm{n}}^{\mathrm{T/R}}, \omega_{\mathrm{n_R}}^{\mathrm{R}}$	wrapped Gaussian	0°, 180°	90°, 90°
$\gamma_{\mathrm{n}}^{\mathrm{T/R}}, \gamma_{\mathrm{n_R}}^{\mathrm{R}}$	wrapped Gaussian	30°, 30°	30°, 30°
$\Delta\omega_{\mathrm{n,m_n}}^{\mathrm{T}}, \Delta\omega_{\mathrm{n,m_n}}^{\mathrm{R}}$	wrapped Gaussian	0°, 0°	1°, 1°
$\Delta\gamma_{\mathrm{n,m_n}}^{\mathrm{T}}, \Delta\gamma_{\mathrm{n,m_n}}^{\mathrm{R}}$	wrapped Gaussian	0°, 0°	1°, 1°
$D_{\mathrm{n}}^{\mathrm{T}}, D_{\mathrm{n}}^{\mathrm{R}}$	exponential	$\frac{1}{50}, \frac{1}{50}$	$\frac{1}{2500}, \frac{1}{2500}$
M_{n}	Poisson	10	10

relative to the Tx/Rx is expressed as

$$\begin{aligned}\vec{C}_{\mathrm{n,m_n}}^{\mathrm{T}}(t) &= \begin{pmatrix} L_{\mathrm{n,m_n}}^{\mathrm{xT}}(t) \\ L_{\mathrm{n,m_n}}^{\mathrm{yT}}(t) \\ L_{\mathrm{n,m_n}}^{\mathrm{zT}}(t) \end{pmatrix} = \begin{pmatrix} L_{\mathrm{n,m_n}}^{\mathrm{xT}}(0) \\ L_{\mathrm{n,m_n}}^{\mathrm{yT}}(0) \\ L_{\mathrm{n,m_n}}^{\mathrm{zT}}(0) \end{pmatrix} + \vec{V}_{\mathrm{n}}^{\mathrm{T}} t \\ &= \begin{pmatrix} D_{\mathrm{n}}^{\mathrm{T}}(0)\cos\gamma_{\mathrm{n,m_n}}^{\mathrm{T}}(0)\cos\omega_{\mathrm{n,m_n}}^{\mathrm{T}}(0) + V_{\mathrm{n}}^{\mathrm{T}}\cos\theta_{\mathrm{n}}^{\mathrm{T}} t \\ D_{\mathrm{n}}^{\mathrm{T}}(0)\cos\gamma_{\mathrm{n,m_n}}^{\mathrm{T}}(0)\sin\omega_{\mathrm{n,m_n}}^{\mathrm{T}}(0) + V_{\mathrm{n}}^{\mathrm{T}}\sin\theta_{\mathrm{n}}^{\mathrm{T}} t \\ D_{\mathrm{n}}^{\mathrm{T}}(0)\sin\gamma_{\mathrm{n,m_n}}^{\mathrm{T}}(0) \end{pmatrix}\end{aligned} \tag{10}$$

$$\begin{aligned}\vec{C}_{\mathrm{n,m_n}}^{\mathrm{R}}(t) &= \begin{pmatrix} L_{\mathrm{n,m_n}}^{\mathrm{xR}}(t) \\ L_{\mathrm{n,m_n}}^{\mathrm{yR}}(t) \\ L_{\mathrm{n,m_n}}^{\mathrm{zR}}(t) \end{pmatrix} \\ &= \begin{pmatrix} D + D_{\mathrm{n}}^{\mathrm{R}}(0)\cos\gamma_{\mathrm{n,m_n}}^{\mathrm{R}}(0)\cos\omega_{\mathrm{n,m_n}}^{\mathrm{R}}(0) \\ D_{\mathrm{n}}^{\mathrm{R}}(0)\cos\gamma_{\mathrm{n,m_n}}^{\mathrm{R}}(0)\sin\omega_{\mathrm{n,m_n}}^{\mathrm{R}}(0) \\ D_{\mathrm{n}}^{\mathrm{R}}(0)\sin\gamma_{\mathrm{n,m_n}}^{\mathrm{R}}(0) \end{pmatrix} + \vec{V}_{\mathrm{n}}^{\mathrm{R}} t\end{aligned} \tag{11}$$

Due to the horizontal V2V motion, the elevation angle trends to 0. The time-variant AAoA of the LoS component is calculated as $\omega_{\mathrm{LoS}}(t) = \arctan\frac{L_{\mathrm{yR}}(t)-L_{\mathrm{yT}}(t)}{L_{\mathrm{xR}}(t)-L_{\mathrm{xT}}(t)}$. Due to the nonlinear characteristic of $\omega_{\mathrm{LoS}}(t)$, When t approximates t_0, the cosine value can be expanded as follows by using the Taylor expansion.

$$\begin{aligned}&\cos\omega_{\mathrm{LoS}}(t) \\ &\approx \cos\omega_{\mathrm{LoS}}(t_0) - \sin\omega_{\mathrm{LoS}}(t_0)\frac{\mathrm{d}\omega_{\mathrm{LoS}}(\mathrm{t})}{\mathrm{d}t}(t-t_0)\end{aligned} \tag{12}$$

where

$$\frac{\mathrm{d}\omega_{\mathrm{LoS}}(\mathrm{t})}{\mathrm{d}t} = \frac{(V_{\mathrm{yR}}(t)-V_{\mathrm{yT}}(t))A_0 - (V_{\mathrm{xR}}(t)-V_{\mathrm{xT}}(t))B_0}{A_0^2+B_0^2} \tag{13}$$

with $A_0 = L_{\mathrm{xR}}(t) - L_{\mathrm{xT}}(t)$ and $B_0 = L_{\mathrm{yR}}(t) - L_{\mathrm{yT}}(t)$.

The time-variant azimuth angle $\omega_{\mathrm{n,m_n}}^{\mathrm{T/R}}(t)$ and elevation angle $\gamma_{\mathrm{n,m_n}}^{\mathrm{T/R}}(t)$ of the m-th ray within the n-th cluster are calculated as

$$\omega_{\mathrm{n,m_n}}^{\mathrm{T/R}}(t) = \begin{cases} \arctan\dfrac{A_{\mathrm{yT/yR}}}{A_{\mathrm{xT/xR}}} (A_{\mathrm{xT/xR}} > 0) \\ \pi + \arctan\dfrac{A_{\mathrm{yT/yR}}}{A_{\mathrm{xT/xR}}} (A_{\mathrm{xT/xR}} \le 0) \end{cases} \tag{14}$$

$$\gamma_{\mathrm{n,m_n}}^{\mathrm{T/R}}(t) = \arctan\frac{L_{\mathrm{n,m_n}}^{\mathrm{zT/zR}}(t)}{\sqrt{A_{\mathrm{xT/xR}}^2 + A_{\mathrm{yT/yR}}^2}} \tag{15}$$

in which $A_{\mathrm{xT/xR}} = L_{\mathrm{n,m_n}}^{\mathrm{xT/xR}}(t) - L_{\mathrm{xT/xR}}(t)$, $A_{\mathrm{yT/yR}} = L_{\mathrm{n,m_n}}^{\mathrm{yT/yR}}(t) - L_{\mathrm{yT/yR}}(t)$. The cosine value can be approximated as

$$\begin{aligned}&\cos\omega_{\mathrm{n,m_n}}^{\mathrm{T/R}}(t) \\ &\approx \cos\omega_{\mathrm{n,m_n}}^{\mathrm{T/R}}(t_0) - \sin\omega_{\mathrm{n,m_n}}^{\mathrm{T/R}}(t_0)\frac{\mathrm{d}\omega_{\mathrm{n,m_n}}^{\mathrm{T/R}}(\mathrm{t})}{\mathrm{d}t}|_{t=t_0}(t-t_0)\end{aligned} \tag{16}$$

$$\begin{aligned}&\cos\gamma_{\mathrm{n,m_n}}^{\mathrm{T/R}}(t) \\ &\approx \cos\gamma_{\mathrm{n,m_n}}^{\mathrm{T/R}}(t_0) - \sin\gamma_{\mathrm{n,m_n}}^{\mathrm{T/R}}(t_0)\frac{\mathrm{d}\gamma_{\mathrm{n,m_n}}^{\mathrm{T/R}}(\mathrm{t})}{\mathrm{d}t}|_{t=t_0}(t-t_0)\end{aligned} \tag{17}$$

where

$$\begin{aligned}&\frac{\mathrm{d}\omega_{\mathrm{n,m_n}}^{\mathrm{T/R}}(\mathrm{t})}{\mathrm{d}t} = \\ &\frac{A_{\mathrm{yT/yR}}(V_{\mathrm{xT/xR}}(t) - V_{\mathrm{n}}^{\mathrm{xT/xR}}) - A_{\mathrm{xT/xR}}(V_{\mathrm{yT/yR}}(t) - V_{\mathrm{n}}^{\mathrm{yT/yR}})}{(A_{\mathrm{xT/xR}}^2 + A_{\mathrm{yT/yR}}^2)}\end{aligned} \tag{18}$$

$$\begin{aligned}&\frac{\mathrm{d}\gamma_{\mathrm{n,m_n}}^{\mathrm{T/R}}(\mathrm{t})}{\mathrm{d}t} \\ &= \frac{M}{\sqrt{A_{\mathrm{xT/xR}}^2 + A_{\mathrm{yT/yR}}^2}(L_{\mathrm{n,m_n}}^{\mathrm{zT/zR}}(t)^2 + A_{\mathrm{xT/xR}}^2 + A_{\mathrm{yT/yR}}^2)}\end{aligned} \tag{19}$$

in which $M = -L_{\mathrm{n,m_n}}^{\mathrm{zT/zR}}(t)[A_{\mathrm{xT/xR}}(V_{\mathrm{xT/xR}}(t) - V_{\mathrm{n}}^{\mathrm{xT/xR}}) + A_{\mathrm{yT/yR}}(V_{\mathrm{yT/yR}}(t) - V_{\mathrm{n}}^{\mathrm{yT/yR}})]$.

The corresponding Doppler frequency of the LoS component and the n-th MB component can be derived as

$$\begin{aligned}f_{\mathrm{LoS}}(t) =& f_{\mathrm{LoS}}^{\mathrm{T}}(t) + f_{\mathrm{LoS}}^{\mathrm{R}}(t) \\ =& \frac{1}{\lambda}\frac{< \vec{L}^{\mathrm{R}}(t) - \vec{L}^{\mathrm{T}}(t), \vec{V}_{\mathrm{T}}(t) - \vec{V}_{\mathrm{R}}(t) >}{||\vec{L}^{\mathrm{R}}(t) - \vec{L}^{\mathrm{T}}(t)||} \\ =& \frac{||V_{\mathrm{T}}||\cos(\omega_{\mathrm{LoS}}(t) - \omega_1 t - \theta_{\mathrm{T}})}{\lambda} \\ &+ \frac{||V_{\mathrm{R}}||\cos(\pi + \omega_{\mathrm{LoS}}(t) - \omega_2 t - \theta_{\mathrm{R}})}{\lambda}\end{aligned} \tag{20}$$

$$\begin{aligned}f_{\mathrm{n,m_n}}(t) =& f_{\mathrm{n,m_n}}^{\mathrm{T}}(t) + f_{\mathrm{n,m_n}}^{\mathrm{R}}(t) \\ =& \frac{1}{\lambda}(< \vec{s}_{\mathrm{n,m_n}}^{\mathrm{T}}(t), \vec{V}_{\mathrm{T}}(t) - \vec{v}_{\mathrm{n}}^{\mathrm{T}} > + < \vec{s}_{\mathrm{n,m_n}}^{\mathrm{R}}(t), \vec{V}_{\mathrm{R}}(t) - \vec{V}_{\mathrm{n}}^{\mathrm{R}} >) \\ =& \frac{1}{\lambda}(||V_{\mathrm{T}}||\cos\gamma_{\mathrm{n,m_n}}^{\mathrm{T}}(t)\cos(\omega_{\mathrm{n,m_n}}^{\mathrm{T}}(t) - \omega_1 t - \theta_{\mathrm{T}}) \\ &+ ||V_{\mathrm{R}}||\cos\gamma_{\mathrm{n,m_n}}^{\mathrm{R}}(t)\cos(\omega_{\mathrm{n,m_n}}^{\mathrm{R}}(t) - \omega_2 t - \theta_{\mathrm{R}}) \\ &- (||V_{\mathrm{n}}^{\mathrm{T}}||\cos\gamma_{\mathrm{n,m_n}}^{\mathrm{T}}(t)\cos(\omega_{\mathrm{n,m_n}}^{\mathrm{T}}(t) - \theta_{\mathrm{n}}^{\mathrm{T}}) \\ &+ ||V_{\mathrm{n}}^{\mathrm{R}}||\cos\gamma_{\mathrm{n,m_n}}^{\mathrm{R}}(t)\cos(\omega_{\mathrm{n,m_n}}^{\mathrm{R}}(t) - \theta_{\mathrm{n}}^{\mathrm{R}}))\end{aligned} \tag{21}$$

Due to the indistinguishability of the delay, rays within each cluster are assumed containing equivalent power. The power of the MPC via the n-th twin-cluster is derived by the

following fomula.

$$\hat{P}_{\mathrm{n}}(t) = e^{-\tau_{\mathrm{n}}(t)\frac{r_\tau - 1}{r_\tau \sigma_\tau}} 10^{-\frac{X}{10}} \tag{22}$$

where X is the shadowing term following Gaussian distribution, i.e., $X \sim N(0,1)$. $\tau_n(t)$ is derived by $\tau_n(t) = (||\vec{L}_{\mathrm{T}}(t) - \vec{C}_{\mathrm{n}}^{\mathrm{T}}(t)|| + ||\vec{C}_{\mathrm{n}}^{\mathrm{T}}(t) - \vec{C}_{\mathrm{n}}^{\mathrm{R}}(t)|| + ||\vec{L}_{\mathrm{R}}(t) - \vec{C}_{\mathrm{n}}^{\mathrm{R}}(t)||)/c + \tau_{\hat{\mathrm{link}}}$, in which c denotes the light speed and $\tau_{\hat{\mathrm{link}}}$ is the virtual delay. $\tau_{\hat{\mathrm{link}}}$ is randomly drawn following $\tau_{\hat{\mathrm{link}}} = -r_\tau \delta_\tau lnu_n$, in which r_τ is the delay scalar, δ_τ is a stochastic delay spread, and u_{n} follows uniform distribution, i.e., $u_{\mathrm{n}} \sim U(0,1)$.

Although the variation of the power comes with the BD process, it is illogical to simulate the power variation by the traditional method mentioned in [31], as the variation of the power is a smooth process. The transition region is introduced to simulate the smooth variation and the transition region for the n-th MPC is computed as [32]

$$\xi_{\mathrm{n}}(t) = \frac{1}{2} - \frac{1}{\pi}\arctan\left(\frac{2\left[L_c + (|2t - T_n| - T_n)||\vec{V}_{\mathrm{T}} - \vec{V}_{\mathrm{R}}||\right]}{\sqrt{\lambda L_c}}\right) \tag{23}$$

where T_n is the lifetime of the n-th cluster. L_c is the duration of the transition process.

Therefore, the normalized power via the n-th twin-cluster can be expressed as

$$P_n(t) = \frac{\xi_{\mathrm{n}}(t)\hat{P}_n(t)}{\sum_{n=1}^{N}\xi_{\mathrm{n}}(t)\hat{P}_n(t)} \tag{24}$$

3. Cluster Evolution Algorithm with Time-Array Consistency

Due to the deployment of MIMO arrays in dynamic scattering scenarios, the channel non-stationarity in time-array domain is seen as a nonnegligible characteristic for V2V channels. The motions of the transceivers and clusters will result in continuous updates of cluster sets within each updated time point, consequently, array evolution is executed for updated clusters. It means that array evolution for antenna sets also needs to satisfy time continuity. Therefore, time evolution and array evolution cannot be seen as isolated evolutionary processes, on the contrary, they have a high degree of coherence. In order to capture non-stationarity for circular moving vehicles, an improved cluster evolution algorithm with time-array consistency is developed.

3.1 Time Evolution

Undoubtedly, the position changes of the transceivers and clusters will produce time-variant channel parameters, which contribute to the dynamic variation of channel properties. The dynamic scattering environment also results in the appearance and disappearance of clusters [33]. It can be explained that when the transceiver escapes from the VR of a cluster, the cluster becomes unobservable. BD process is regarded as a general method to simulate cluster evolution in time domain. The birth rate and death rate are λ_{B} and λ_{D}, respectively. The survival probability of the n-th cluster can be calculated as

$$P_{\mathrm{sur}}(\Delta t) = e^{-\frac{\lambda_{\mathrm{D}}(V_{\mathrm{T}} + V_{\mathrm{R}} + P_{\mathrm{c}}(V_{\mathrm{n}}^{\mathrm{T}} + V_{\mathrm{n}}^{\mathrm{R}}))\Delta t}{D_{\mathrm{c}}}} \tag{25}$$

where $P_{\mathrm{c}} \in [0,1]$ represents the influencing factor of the n-th twin cluster and D_{c} is a scenario dependent factor.

Considering that each cluster has its unique survival probability, mean survival probability can be calculated as $P_{\mathrm{sur}}(\Delta t) = \frac{\sum_{n=1}^{N(t)} P_{\mathrm{sur}}^{\mathrm{n}}(\Delta t)}{N(t)}$. New twin clusters are generated obeying Poisson distribution, which is written as $E(N_{\mathrm{new}}(t + \Delta t)) = \frac{\lambda_{\mathrm{B}}}{\lambda_{\mathrm{D}}}(1 - P_{\mathrm{sur}}(\Delta t))$. The initial number of twin clusters is calculated as $N(t_0) = \frac{\lambda_{\mathrm{B}}}{\lambda_{\mathrm{D}}}$. A general BD method is verified to effectively simulate time evolution in the high-mobility and linear motion scenario, in which disappeared clusters cannot reappear [32], [34], [35]. However, low-speed curved moving vehicles and the presence of a number of uncertain dynamic clusters with arbitrary velocities and directions may lead to the disappeared clusters becoming observable again in a short period of time for complex urban scenes. For example, the movement of obstacles away from static clusters and the movement of dynamic clusters away from static obstacles in a short time will both contribute to the rebirth phenomenon. Therefore, we define that $E(N_{\mathrm{new}}(t + \Delta t))$ describes the sum of new clusters and rebirth clusters at time point $t + \Delta t$ in the proposed algorithm.

Figure 3 shows an example of cluster evolution process as well as the normalized power variation in time domain. At the initial time, there are 10 observable clusters. As time goes by, the power of some clusters gets to 0, which means these clusters become unobservable or in other words, these clusters are dead. The power of some dead clusters increases from 0, which indicates dead clusters become observable again or in other words, these clusters are reborn. For the cluster with an index greater than 10, the power of clusters increases from 0 at some points, which means new clusters are born with time. Therefore, clusters contain birth, death, and rebirth characteristics. In addition, the power is constantly changing as the motion of the transceivers and clusters. The

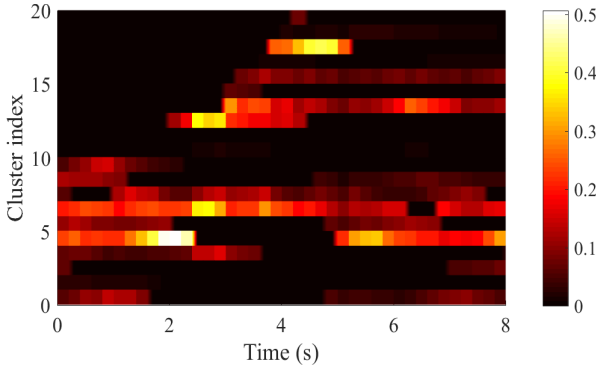

Fig. 3 An example of normalized power variation in time domain. (λ_{B}=1, λ_{D}=0.1).

disappearance and appearance of clusters are not instantaneous, as it is perceptible that the power gradually decreases to zero or increases from zero.

3.2 Array Evolution

For massive MIMO, spatial non-stationarity is always reflected that each cluster has a unique antenna set. It can be proved that each antenna also has a VR, and different spatial locations will lead to differences in observable cluster sets. BD method is also widely used to describe array evolution [34], [36], [37]. Considering that the time-array consistency should persistently be guaranteed, the method has limitations to apply to transceivers in circular motions. One reason is that antenna sets of the static cluster become more similar to the initial antenna sets as the vehicle with circular motion approaches its initial position. In a more extreme case, when the vehicle coincides with its initial position, the static cluster will still be observed collectively. Therefore, a novel method suitable for the scenario is proposed to simulate the dynamic and static antenna sets of circular moving vehicles. In principle, each antenna has a VR with similar size [35] and thus, adjacent antennas will share a large VR, which means antenna set for each cluster satisfies continuity. In order to satisfy the time-array coherence, the whole process of the proposed algorithm can be developed as follows.

Step 1: An initial cluster set is generated at time t.

Step 2: Taking the transmitting antennas for example, the initial transmitting antenna p for the array evolution of the n-th cluster is derived obeying uniform distribution, i.e., $p \sim \mathrm{U}(1, M_{\mathrm{T}})$.

Step 3: Calculate the distance $d_{\mathrm{p,C_n^T}}$ from the n-th cluster to the p-th transmitting antenna, i.e., $d_{\mathrm{p,C_n^T}} = ||\vec{C}^{\mathrm{T}}_{\mathrm{n,m_n}}(t) - \vec{L}_{\mathrm{xT}}(t) - \vec{A}^{\mathrm{T}}_{\mathrm{p}}(t)||$.

Step 4: Calculate the distance $d_{\mathrm{p_1p}}$ from the p_1-th ($p_1 \in [1, M_{\mathrm{T}}], p_1 \in N^+$) antenna to the p-th antenna and compare $\frac{d_{\mathrm{p,C_n^T}}}{U_{\mathrm{T/R}}}$ and $d_{\mathrm{p_1p}}$. If $\frac{d^{\mathrm{T}}_{\mathrm{p,n}}}{U_{\mathrm{T/R}}} \le d_{\mathrm{p_1p}}$, the p_1-th antenna can observe the n-th cluster. $U_{\mathrm{T/R}}$ is defined as the shrinkage factors.

Step 5: Time evolution for survival clusters at time point $t + \Delta t$ based on the survival probability P_{sur}.

Step 6: Time evolution for new clusters and rebirth clusters at time point $t + \Delta t$. If $E(N_{\mathrm{new}}(t + \Delta t)) > 0$, $E(N_{\mathrm{new}}(t + \Delta t))$ clusters are distributed to new generated clusters and rebirth clusters obeying uniform distribution.

In addition, the updated location of the survival cluster is derived in Eq. (10) and Eq. (11). For the rebirth cluster $C_{\mathrm{n}}^{\mathrm{T/R}}$ at time point $t+\Delta t$, it is assumed that the first generation of the cluster is at time point t_1. The location of the rebirth cluster can be calculated as $\vec{C}_{\mathrm{n}}^{\mathrm{T/R}}(t+\Delta t) = \vec{C}_{\mathrm{n}}^{\mathrm{T/R}}(t_1)+\vec{V}_{\mathrm{n}}^{\mathrm{T/R}}(t+\Delta t - t_1)$. For newly generated cluster $C_{\mathrm{n+1}}^{\mathrm{T/R}}$, the location can be calculated according to Table 1.

In order to visually present the effect of circular motion on MIMO arrays, array evolutions for static clusters and dynamic clusters are respectively explored at different time points in Fig. 4. It can be observed that the number of

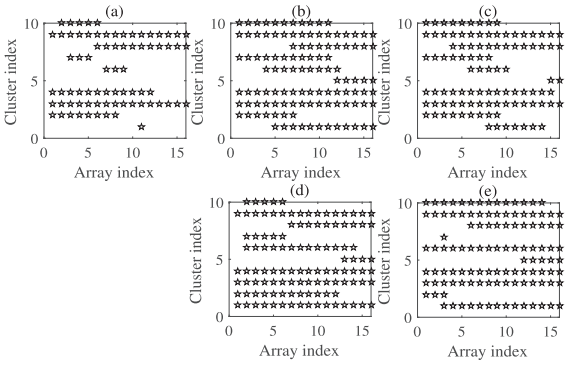

Fig. 4 Array evolution of cluster types at different time point. (a) Dynamic or static clusters (t=0 s), (b) static clusters (t=5 s), (c) static clusters (t=8 s), (d) dynamic clusters (t=5 s), (e) dynamic clusters (t=8 s).

MIMO antennas is 20 and 10 clusters are observed. By comparing (a), (b), (c) and (a), (d), (e) along time separately, it can be found that each antenna has a unique cluster set, which changes over time. It can also be seen that when the Tx or Rx maintains a fixed angular velocity consistently, static cluster sets become more similar to the initial cluster sets ($t = 0$) over time. By contrast, dynamic cluster sets show significant changes compared to the initial cluster sets ($t = 0$). It is because the dynamism of clusters leads to greater distance and location variation, therefore results in more drastic array evolution. Additionally, certain dynamic clusters will maintain a greater distance from the transceiver over time and can probably be observed by the entire MIMO.

4. Statistical Properties

4.1 ST-CF

The normalized ST-CF is defined as

$$R_{\mathrm{pq,p'q'}}(t, \Delta t) = \frac{E[h_{\mathrm{pq}}(t)h^*_{\mathrm{pq}}(t + \Delta t)]}{\sqrt{E[\left|h_{\mathrm{pq}}(t)\right|^2]E[\left|h_{\mathrm{pq}}(t + \Delta t)\right|^2]}} \tag{26}$$

Since twin-clusters are assumed independent, the ST-CF can be split into the ST-CF of the LoS component and the ST-CF of MB components as follows.

$$R_{\mathrm{pq,p'q'}}(t, \Delta t) = R^{\mathrm{LoS}}_{\mathrm{pq,p'q'}}(t, \Delta t) + \sum_{n=1}^{N} R^{\mathrm{n}}_{\mathrm{pq,p'q'}}(t, \Delta t) \tag{27}$$

The ST-CF of the LoS component is computed as

$$R^{\mathrm{LoS}}_{\mathrm{pq,p'q'}}(t, \Delta t) = \frac{K}{K+1} e^{j2\pi(\Phi^{\mathrm{T,LoS}}(t)+\Phi^{\mathrm{R,LoS}}(t))+j2\pi/\lambda(\Psi^{\mathrm{T,LoS}}_{\mathrm{pp'}}(t)+\Psi^{\mathrm{R,LoS}}_{\mathrm{qq'}}(t))} \tag{28}$$

where

$$\Psi^{\mathrm{T,LoS}}_{\mathrm{pp'}}(t) = k_{\mathrm{p}}\delta_{\mathrm{T}}(\cos\alpha_{\mathrm{T}}\cos(\beta_{\mathrm{T}} - \omega_{LoS}(t + \Delta t)) - k_{\mathrm{p'}}\delta_{\mathrm{T}}(\cos\alpha_{\mathrm{T}}\cos(\beta_{\mathrm{T}} - \omega_{LoS}(t)) \tag{29}$$

$$
\begin{aligned}
\Phi^{\mathrm{T}}_{\mathrm{n},\mathrm{m_n}}(t) &= \int_t^{t+\Delta t} \frac{||V_{\mathrm{T}}||}{\lambda}(\cos\gamma^{\mathrm{T}}_{\mathrm{n},\mathrm{m_n}}(t')\cos(\omega^{\mathrm{T}}_{\mathrm{n},\mathrm{m_n}}(t')-\omega_1 t-\theta_{\mathrm{T}})) - \frac{||V^{\mathrm{T}}_{\mathrm{n}}||}{\lambda}(\cos\gamma^{\mathrm{T}}_{\mathrm{n},\mathrm{m_n}}(t')\cos(\omega^{\mathrm{T}}_{\mathrm{n},\mathrm{m_n}}(t')-\theta_{\mathrm{T}}))dt' \\
&\approx \int_t^{t+\Delta t} \frac{||V_{\mathrm{T}}||}{\lambda}((\cos\gamma^{\mathrm{T}}_{\mathrm{n},\mathrm{m_n}}(t) - \sin\gamma^{\mathrm{T}}_{\mathrm{n},\mathrm{m_n}}(t)\frac{d\gamma^{\mathrm{T}}_{\mathrm{n},\mathrm{m_n}}(t')}{dt}|_{t'=t}(t'-t))(\cos(\omega^{\mathrm{T}}_{\mathrm{n},\mathrm{m_n}}(t)-\omega_1 t-\theta_{\mathrm{T}}) \\
&- \sin(\omega^{\mathrm{T}}_{\mathrm{n},\mathrm{m_n}}(t)-\omega_1 t-\theta_{\mathrm{T}})(\frac{d\omega^{\mathrm{T}}_{\mathrm{n},\mathrm{m_n}}(t')}{dt'}|_{t'=t}-\omega_1)(t'-t)) - \frac{||V^{\mathrm{T}}_{\mathrm{n}}||}{\lambda}((\cos\gamma^{\mathrm{T}}_{\mathrm{n},\mathrm{m_n}}(t) - \sin\gamma^{\mathrm{T}}_{\mathrm{n},\mathrm{m_n}}(t)\frac{d\gamma^{\mathrm{T}}_{\mathrm{n},\mathrm{m_n}}(t')}{dt}|_{t'=t}(t'-t)) \\
&(\cos(\omega^{\mathrm{T}}_{\mathrm{n},\mathrm{m_n}}(t)-\theta_{\mathrm{T}}) - \sin(\omega^{\mathrm{T}}_{\mathrm{n},\mathrm{m_n}}(t)-\theta_{\mathrm{T}})(\frac{d\omega^{\mathrm{T}}_{\mathrm{n},\mathrm{m_n}}(t')}{dt'}|_{t'=t})(t'-t)) \\
&\approx \int_0^{\Delta t} \frac{||V_{\mathrm{T}}||}{\lambda}((\cos\gamma^{\mathrm{T}}_{\mathrm{n},\mathrm{m_n}}(t) - \sin\gamma^{\mathrm{T}}_{\mathrm{n},\mathrm{m_n}}(t)\frac{d\gamma^{\mathrm{T}}_{\mathrm{n},\mathrm{m_n}}(t')}{dt}|_{t'=t}u)(\cos(\omega^{\mathrm{T}}_{\mathrm{n},\mathrm{m_n}}(t)-\omega_1 t-\theta_{\mathrm{T}}) \\
&- \sin(\omega^{\mathrm{T}}_{\mathrm{n},\mathrm{m_n}}(t)-\omega_1 t-\theta_{\mathrm{T}})(\frac{d\omega^{\mathrm{T}}_{\mathrm{n},\mathrm{m_n}}(t')}{dt'}|_{t'=t}-\omega_1)u) - \frac{||V^{\mathrm{T}}_{\mathrm{n}}||}{\lambda}((\cos\gamma^{\mathrm{T}}_{\mathrm{n},\mathrm{m_n}}(t) - \sin\gamma^{\mathrm{T}}_{\mathrm{n},\mathrm{m_n}}(t)\frac{d\gamma^{\mathrm{T}}_{\mathrm{n},\mathrm{m_n}}(t')}{dt}|_{t'=t}u) \\
&(\cos(\omega^{\mathrm{T}}_{\mathrm{n},\mathrm{m_n}}(t)-\theta_{\mathrm{T}}) - \sin(\omega^{\mathrm{T}}_{\mathrm{n},\mathrm{m_n}}(t)-\theta_{\mathrm{T}})\frac{d\omega^{\mathrm{T}}_{\mathrm{n},\mathrm{m_n}}(t')}{dt'}|_{t'=t})u)du \\
&\approx \int_0^{\Delta t} \frac{||V_{\mathrm{T}}||}{\lambda}(M_1-N_1u)(M_2-N_2u) - \frac{||V^{\mathrm{T}}_{\mathrm{n}}||}{\lambda}(M_1-N'_1u)(M_2-N'_2u)du \\
&\approx \frac{||V_{\mathrm{T}}||}{\lambda}(M_1M_2\Delta t - \frac{1}{2}(M_2N_1+M_1N_2)\Delta t^2 + \frac{1}{3}N_1N_2\Delta t^3) - \frac{||V^{\mathrm{T}}_{\mathrm{n}}||}{\lambda}(M_1M_2\Delta t - \frac{1}{2}(M_2N'_1+M_1N'_2)\Delta t^2 + \frac{1}{3}N'_1N'_2\Delta t^3)
\end{aligned} \tag{34}
$$

$$
\begin{aligned}
&\Psi^{\mathrm{R,LoS}}_{\mathrm{qq'}}(t) = k_{\mathrm{q}}\delta_{\mathrm{R}}(\cos\alpha_{\mathrm{R}}\cos(\pi+\beta_{\mathrm{R}}-\omega_{LoS}(t+\Delta t)) \\
&-k_{\mathrm{q'}}\delta_{\mathrm{R}}(\cos\alpha_{\mathrm{R}}\cos(\pi+\beta_{\mathrm{R}}-\omega_{LoS}(t))
\end{aligned} \tag{30}
$$

$$
\Phi^{\mathrm{T,LoS}}(t) = \int_t^{t+\Delta t} f^{\mathrm{T,LoS}}(t')dt' \tag{31}
$$

$$
\Phi^{\mathrm{R,LoS}}(t) = \int_t^{t+\Delta t} f^{\mathrm{R,LoS}}(t')dt' \tag{32}
$$

By introducing the BD process, the survival probability of each MB component follows the exponential distribution. It needs to be mentioned that when one MB component becomes unobservable, the corresponding CIR and ST-CF equal 0. Therefore, combined with the BD process, the ST-CF of the n-th MB component can be derived as

$$
\begin{aligned}
&R^{\mathrm{n}}_{\mathrm{pq,p'q'}}(t,\Delta t) = \frac{\sqrt{P_{\mathrm{n}}(t)P_{\mathrm{n}}(t+\Delta t)}}{K+1}p^{\mathrm{n}}_{\mathrm{sur}}(\Delta t) \\
&e^{j2\pi(\Phi^{\mathrm{T}}_{\mathrm{n},\mathrm{m_n}}(t)+\Phi^{\mathrm{R}}_{\mathrm{n},\mathrm{m_n}}(t))}e^{j2\pi/\lambda(\Psi^{\mathrm{T}}_{\mathrm{pp'}}(t)+\Psi^{\mathrm{R}}_{\mathrm{qq'}}(t))}
\end{aligned} \tag{33}
$$

where $\Phi^{\mathrm{T}}_{\mathrm{n},\mathrm{m_n}}(t) = \int_t^{t+\Delta t} f^{\mathrm{T}}_{\mathrm{n},\mathrm{m_n}}(t')dt'$ and $\Phi^{\mathrm{R}}_{\mathrm{n},\mathrm{m_n}}(t) = \int_t^{t+\Delta t} f^{\mathrm{R}}_{\mathrm{n},\mathrm{m_n}}(t')dt'$. $\Psi^{\mathrm{T}}_{\mathrm{pp'}}(t) = A^{\mathrm{T}}_{\mathrm{p}}(t+\Delta t)s^{T}_{\mathrm{n},\mathrm{m_n}}(t+\Delta t) - A^{\mathrm{T}}_{\mathrm{p'}}(t)s^{T}_{\mathrm{n},\mathrm{m_n}}(t)$, $\Psi^{\mathrm{R}}_{\mathrm{qq'}}(t) = A^{\mathrm{R}}_{\mathrm{q}}(t+\Delta t)s^{R}_{\mathrm{n},\mathrm{m_n}}(t+\Delta t) - A^{\mathrm{R}}_{\mathrm{q'}}(t)s^{R}_{\mathrm{n},\mathrm{m_n}}(t)$.

The detailed derivation of $\Phi^{\mathrm{T}}_{\mathrm{n},\mathrm{m_n}}(t)$ is shown in (34), in which $M_1 = \cos\gamma^{\mathrm{T}}_{\mathrm{n},\mathrm{m_n}}(t)$, $M_2 = \cos(\gamma^{\mathrm{T}}_{\mathrm{n},\mathrm{m_n}}(t)-\omega_1 t-\theta_{\mathrm{T}})$, $N_1 = -\sin\gamma^{\mathrm{T}}_{\mathrm{n},\mathrm{m_n}}(t)\frac{d\gamma^{\mathrm{T}}_{\mathrm{n},\mathrm{m_n}}(t')}{dt}|_{t'=t}$, and $N_2 = -\sin(\omega^{\mathrm{T}}_{\mathrm{n},\mathrm{m_n}}(t)-\omega_1 t-\theta_{\mathrm{T}})(\frac{d\omega^{\mathrm{T}}_{\mathrm{n},\mathrm{m_n}}(t'-\omega_1 t-\theta_{\mathrm{T}})}{dt'}|_{t'=t})$, $N'_1 = \sin(\gamma^{\mathrm{T}}_{\mathrm{n},\mathrm{m_n}}(t)-\theta_{\mathrm{T}})$, and $N'_2 = -\sin(\omega^{\mathrm{T}}_{\mathrm{n},\mathrm{m_n}}(t)-\theta_{\mathrm{T}})(\frac{d\omega^{\mathrm{T}}_{\mathrm{n},\mathrm{m_n}}(t'-\theta_{\mathrm{T}})}{dt'}|_{t'=t})$.

Analogously, $\Phi^{\mathrm{R}}_{\mathrm{n},\mathrm{m_n}}(t)$ is expressed as

$$
\begin{aligned}
&\Phi^{\mathrm{R}}_{\mathrm{n},\mathrm{m_n}}(t) \approx \\
&\frac{||V_{\mathrm{R}}||}{\lambda}(M_3M_4\Delta t - \frac{1}{2}(M_3N_4+M_4N_3)\Delta t^2 + \frac{1}{3}N_3N_4\Delta t^3) \\
&- \frac{||V^{\mathrm{R}}_{\mathrm{n}}||}{\lambda}(M_3M_4\Delta t - \frac{1}{2}(M_3N'_4+M_4N'_3)\Delta t^2 + \frac{1}{3}N'_3N'_4\Delta t^3)
\end{aligned} \tag{35}
$$

in which $M_3 = \cos\gamma^{\mathrm{R}}_{\mathrm{n},\mathrm{m_n}}(t)$, $N_3 = \sin(\gamma^{\mathrm{R}}_{\mathrm{n},\mathrm{m_n}}(t)-\omega_2 t-\theta_{\mathrm{R}})$, $M_4 = -\sin\gamma^{\mathrm{R}}_{\mathrm{n},\mathrm{m_n}}(t)\frac{d\gamma^{\mathrm{R}}_{\mathrm{n},\mathrm{m_n}}(t')}{dt}|_{t'=t}$, $N_4 = -\sin(\omega^{\mathrm{R}}_{\mathrm{n},\mathrm{m_n}}(t)-\omega_1 t-\theta_{\mathrm{R}})(\frac{d\omega^{\mathrm{R}}_{\mathrm{n},\mathrm{m_n}}(t'-\omega_1 t-\theta_{\mathrm{R}})}{dt'}|_{t'=t})$, $N'_3 = \sin(\gamma^{\mathrm{R}}_{\mathrm{n},\mathrm{m_n}}(t)-\theta_{\mathrm{R}})$, and $N'_4 = -\sin(\omega^{\mathrm{R}}_{\mathrm{n},\mathrm{m_n}}(t)-\theta_{\mathrm{R}})(\frac{d\omega^{\mathrm{R}}_{\mathrm{n},\mathrm{m_n}}(t'-\theta_{\mathrm{R}})}{dt'}|_{t'=t})$.

In addition, $\Psi^{\mathrm{T}}_{\mathrm{pp'}}(t)$ and $\Psi^{\mathrm{R}}_{\mathrm{qq'}}(t)$ can be simplified as follows.

$$
\begin{aligned}
&\Psi^{\mathrm{T}}_{\mathrm{pp'}}(t) = k_{\mathrm{p}}\delta_{\mathrm{T}}(\cos\alpha_{\mathrm{T}}\cos\gamma^{\mathrm{T}}_{\mathrm{n},\mathrm{m_n}}(t+\Delta t)\cos(\omega_1(t+\Delta t) \\
&+\beta_{\mathrm{T}}-\omega^{\mathrm{T}}_{\mathrm{n},\mathrm{m_n}}(t+\Delta t)) + \sin\alpha_{\mathrm{T}}\sin\gamma^{\mathrm{T}}_{\mathrm{n},\mathrm{m_n}}(t+\Delta t)) \\
&- k_{\mathrm{p'}}\delta_{\mathrm{T}}(\cos\alpha_{\mathrm{T}}\cos\gamma^{\mathrm{T}}_{\mathrm{n},\mathrm{m_n}}(t)\cos(\omega_1 t+\beta_{\mathrm{T}}-\omega^{\mathrm{T}}_{\mathrm{n},\mathrm{m_n}}(t)) \\
&- \sin\alpha_{\mathrm{T}}\sin\gamma^{\mathrm{T}}_{\mathrm{n},\mathrm{m_n}}(t))
\end{aligned} \tag{36}
$$

$$
\begin{aligned}
&\Psi^{\mathrm{R}}_{\mathrm{qq'}}(t) = k_{\mathrm{q}}\delta_{\mathrm{R}}(\cos\alpha_{\mathrm{R}}\cos\gamma^{\mathrm{R}}_{\mathrm{n},\mathrm{m_n}}(t+\Delta t)\cos(\omega_2(t+\Delta t) \\
&+\beta_{\mathrm{R}}-\omega^{\mathrm{R}}_{\mathrm{n},\mathrm{m_n}}(t+\Delta t)) + \sin\alpha_{\mathrm{R}}\sin\gamma^{\mathrm{R}}_{\mathrm{n},\mathrm{m_n}}(t+\Delta t)) \\
&- k_{\mathrm{q'}}\delta_{\mathrm{R}}(\cos\alpha_{\mathrm{R}}\cos\gamma^{\mathrm{R}}_{\mathrm{n},\mathrm{m_n}}(t)\cos(\omega_2 t+\beta_{\mathrm{R}}-\omega^{\mathrm{R}}_{\mathrm{n},\mathrm{m_n}}(t)) \\
&- \sin\alpha_{\mathrm{R}}\sin\gamma^{\mathrm{R}}_{\mathrm{n},\mathrm{m_n}}(t))
\end{aligned} \tag{37}
$$

4.2 Doppler PSD

Doppler PSD can be calculated by the Fourier transform of $R_{\mathrm{pq,p'q'}}(t,\Delta t)$, which can be written as

$$S_{\mathrm{pq}}(t,f)=\int_{-\infty}^{\infty}R_{\mathrm{pq}}(t,\Delta t)e^{-j2\pi f\Delta t}d\Delta t \tag{38}$$

4.3 Quasi-Stationary Interval

Quasi-stationary interval is explored to calculate the maximum duration, over which the condition of wide-sense stationary is valid. Quasi-stationary interval can be defined as the shortest duration T_{S}, over which the relative error value of the absolute value Doppler spread at time instant T_{S} relative to the initial time instant 0 equals s. It can be written as [20]

$$s=\frac{|B_{\mathrm{pq}}(T_{\mathrm{S}})-B_{\mathrm{pq}}(0)|}{B_{\mathrm{pq}}(0)} \tag{39}$$

where $B_{\mathrm{pq}}(T_{\mathrm{S}})$ denotes the Doppler spread at time instant T_{S}, which is calculated by

$$B_{\mathrm{pq}}(T_{\mathrm{S}})=\frac{1}{2\pi}\sqrt{(\frac{\dot{R}_{\mathrm{pq}}(t,\Delta t)|_{\Delta t=0}}{R_{\mathrm{pq}}(t,0)})^2-\frac{\ddot{R}_{\mathrm{pq}}(t,\Delta t)|_{\Delta t=0}}{R_{\mathrm{pq}}(t,0)}} \tag{40}$$

$\dot{R}_{\mathrm{pq}}(t,\Delta t)$ and $\ddot{R}_{\mathrm{pq}}(t,\Delta t)$ are the first and second order derivative of $R_{\mathrm{pq}}(t,\Delta t)$ with respect to Δt, at $\Delta t=0$. And we consider the channel is quasi-stationary in the time interval $(0,T_{\mathrm{S}}]$ when $s\le 0.1$.

4.4 Instantaneous Doppler Frequency and RMS Doppler Spread

The movement of the vehicles and clusters as well as the rotates of ULAs will result in dynamic changes of Doppler frequencies. The Doppler frequency of the m-th ray within the n-th cluster can be calculated as

$$f_{\mathrm{n,m_n}}(t)=\frac{1}{\lambda}\frac{\mathrm{d}(\Phi^{\mathrm{T}}_{\mathrm{n,m_n}}(t)+\Phi^{\mathrm{R}}_{\mathrm{n,m_n}}(t)+\Psi^{\mathrm{T}}_{\mathrm{pp'}}(t)+\Psi^{\mathrm{R}}_{\mathrm{qq'}}(t))}{\mathrm{d}t} \tag{41}$$

The RMS Doppler spread is used to characterize the dispersion of the signal in Doppler frequency domain. The RMS Doppler spread δ_{f} is calculated as

$$\delta_{\mathrm{f}}=\sqrt{\overline{f_{\mathrm{d}}^2}-\overline{f_{\mathrm{d}}}^2} \tag{42}$$

where

$$\overline{f_{\mathrm{d}}^2}=\sum_{n=1}^{N}\sum_{m_n=1}^{M_n}\frac{P_{\mathrm{n,m_n}}(t)}{M_n}f^2_{\mathrm{n,m_n}}(t) \tag{43}$$

$$\overline{f_{\mathrm{d}}}=\sum_{n=1}^{N}\sum_{m_n=1}^{M_n}\frac{P_{\mathrm{n,m_n}}(t)}{M_n}f_{\mathrm{n,m_n}}(t) \tag{44}$$

4.5 Delay PSD and Angular PSD

The delay PSD and the angular PSD intuitively reveal the power distribution in time delay domain and in angular domain as follows.

$$\Lambda(t,\tau)=\frac{K}{K+1}\delta(\tau-\tau_{\mathrm{LoS}}(t))+\sum_{n=1}^{\mathrm{N(t)}}\frac{P_{\mathrm{n}}(t)}{K+1}\delta(\tau-\tau_{\mathrm{n}}(t)) \tag{45}$$

$$\Psi(t,\mu)=\frac{K}{K+1}\delta(\mu-\mu_{\mathrm{LoS}})+\sum_{n=1}^{\mathrm{N(t)}}\frac{P_{\mathrm{n}}(t)}{K+1}\delta(\mu-\mu^{\mathrm{T}}_{\mathrm{n}}(t)) \tag{46}$$

where μ_{LoS} and $\mu^{\mathrm{T}}_{\mathrm{n}}(t)$ denote the AoD of the LoS component and the AoD of the n-th MB component, respectively.

5. Numerical Results and Analysis

In this section, the statistical properties of the proposed channel model are investigated. Although faster signal attenuation and shorter coverage distance for larger frequency, the V2V communication distance is below kilometer level in the model and thus, the requirement for transmission distance is relatively low. Therefore, the frequencies from the 2.4–2.5 GHz to Ku band range can be applied to the model. Due to 5.9 GHz being commonly used for V2V communications, we set $f=5.9$ GHz. Some of the parameters are shown in Table 1. Other parameters are set as $D=300$ m, $V_{\mathrm{T}}=10$ m/s, $\theta_{\mathrm{T}}=\frac{\pi}{3}$, $\omega_1=\frac{\pi}{6}$ rad/s, $V_{\mathrm{R}}=10$ m/s, $\theta_{\mathrm{R}}=-\frac{\pi}{3}$, $\omega_2=-\frac{\pi}{5}$ rad/s, $\alpha_{\mathrm{T}}=\frac{\pi}{4}$, $\beta_{\mathrm{T}}=\frac{\pi}{4}$, $\alpha_{\mathrm{R}}=\frac{\pi}{4}$, $\beta_{\mathrm{R}}=\frac{\pi}{4}$, $\delta_{\mathrm{T}}=\frac{\lambda}{2}$, $\delta_{\mathrm{R}}=\frac{\lambda}{2}$, $r_\tau=2.1$, $\delta=10^{-7}$, $N=20$. Considering the randomness of cluster movements, we set $\theta^{\mathrm{T}}_{\mathrm{n}}\sim\mathrm{U}(0,2\pi)$, $\theta^{\mathrm{R}}_{\mathrm{n}}\sim\mathrm{U}(0,2\pi)$. For low dynamic scattering environments, scatterers are mainly composed of pedestrians, moving bicycles, and buildings. Therefore, moving clusters remain at lower speeds, usually not exceeding 5 m/s. We set $V^{\mathrm{T}}_{\mathrm{n}}\sim\mathrm{U}(0,5)\,m/s$, $V^{\mathrm{R}}_{\mathrm{n}}\sim\mathrm{U}(0,5)$ m/s. For high dynamic scattering environments, more clusters are composed of moving vehicles. Therefore, we set $V^{\mathrm{T}}_{\mathrm{n}}\sim\mathrm{U}(0,15)\,m/s$, $V^{\mathrm{R}}_{\mathrm{n}}\sim\mathrm{U}(0,15)$ m/s.

By setting $p=p'$, $q=q'$, the temporal auto-correlation function (ACF) $R_{\mathrm{pq}}(t,\Delta t)$ can be derived in Fig. 5. It can be seen that the temporal ACFs change over time, which verifies the channel non-stationarity in time domain. The time-variation characteristic of the temporal ACF is the result of the simultaneous action of time-variant channel parameters and time evolution process. In addition, the temporal ACF of linear motion in low dynamic scattering environments becomes larger with time. Compared with linear motion,

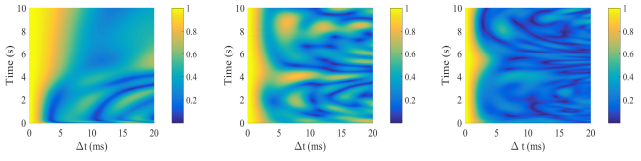

Fig. 5 Temporal ACFs with different time. (a) Linear motion, low dynamic clusters. (b) Circular motion, low dynamic clusters. (c) Circular motion, high dynamic clusters.

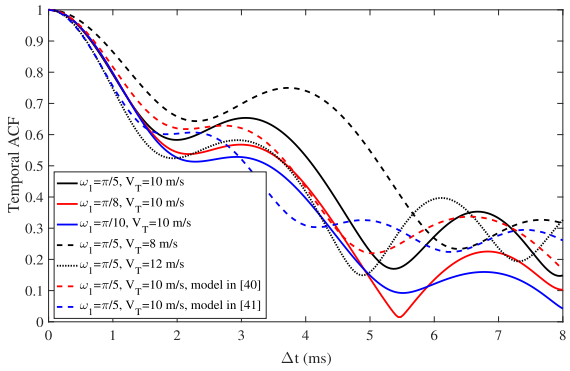

Fig. 6 Temporal ACFs with different angular velocities and moving velocities at $t = 1s$. For model in [40], the parameters are set as $R_{\mathrm{t}} = R_{\mathrm{r}} = 20\,m$, $\eta_{SB_1} = 0.4$, $\eta_{SB_2} = 0.4$, $\eta_{SB_3} = 0.1$, $\eta_{DB} = 0.1$, $k^1 = 10$, $k^2 = 10$, $k^3 = 10$, $\alpha_{\mathrm{T0}}^{(1)} = \pi$, $\alpha_{\mathrm{T0}}^{(2)} = \frac{3\pi}{10}$, $\alpha_{\mathrm{T0}}^{(3)} = \frac{\pi}{10}$, $\beta_{\mathrm{T0}}^{(1)} = 0$, $\beta_{\mathrm{T0}}^{(2)} = \frac{2\pi}{5}$, $\beta_{\mathrm{T0}}^{(3)} = \frac{\pi}{10}$. Model in [41] shares the same parameters as the model in [40]. Other parameters are consistent with the proposed model.

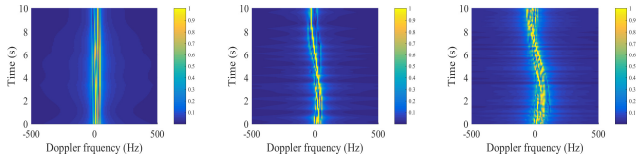

Fig. 7 Normalized Doppler PSD with different time. (a) Linear motion, low dynamic clusters. (b) Circular motion, low dynamic clusters. (c) Circular motion, high dynamic clusters.

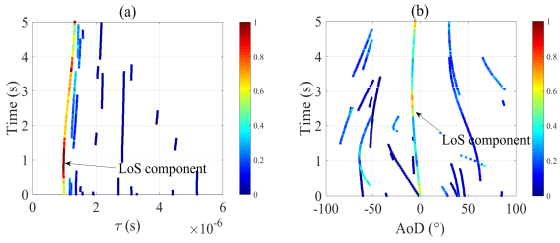

Fig. 8 Delay PSD and angular PSD.

circular motion generates non-monotonic changes of temporal ACFs with time and it has a trend of getting large first and then becoming small. It can be explained that when the vehicle moves away from clusters, a small angular spread of the AoDs or AoAs leads to a large temporal ACF. Unlike linear motion with unitary approach or away from clusters, circular motion involves both processes. Therefore, the moving pattern can affect the time correlation. Similar to low dynamic scattering environments, the changing trend can also be perceived in high dynamic scattering environments (c). It can also be found that compared with (a) and (b), the temporal ACF remains significantly smaller in (c). Therefore, we can conclude that dynamic clusters contribute to the decrease of the temporal ACF. That's because randomly generated velocities and directions of clusters contribute to a large Doppler spread.

Figure 6 presents temporal ACFs for different angular velocities and moving velocities at $t = 1s$. It can be seen that the temporal ACF is larger as the increase of angular velocity. Since a larger angular velocity means that the vehicle has a greater steering, it generates a larger change of angular spread and thus, has a significant impact on the time correlation. In addition, the conclusion that a large moving speed will lead to a small temporal ACF [38] also holds in curved motion. It is result from a wider Doppler spread and more drastic changes of channel parameters caused by a larger moving speed. Moreover, the proposed model is compared with the model in [40] and [41]. In [40], a two-sphere model and a cylinder model are combined to simulate the local and far scattering environment. In [41], a two-ring model and an ellipse model are combined to model the scattering environment. Considering that the complex scattering environment including far scatterers and local scatterers is simulated by clusters with different distribution in the proposed model, the scattering scenario is similar to the scenario in [40] and [41]. It can be seen that by adjusting the channel parameters, the temporal ACFs of the RS GBSMs in [40] and [41] share similar downtrends with the proposed model, which verifies the reasonability and usability of the proposed model. Owing to the 2D model in [41], elevation angles are neglected. Therefore, the temporal ACF in [40] has a higher similarity with the proposed model than the temporal ACF in [41].

The normalized Doppler PSD $S_{\mathrm{pq}}(t, f)$ with different time is shown in Fig. 7. The Doppler PSD shows a strong linear variation with time in (a), which is consistent with the linear motion mode. By comparison, circular movement can present a clear curvilinear change of the peak in (b). The largest peak of the Doppler PSD also has a trend of increasing first and then decreasing. The phenomenon that the time-variant Doppler PSD changes with the motion mode can also be observed in [39]. Additionally, other peaks with less power show different changing trajectories over time. This is due to the uneven variation of channel parameters caused by curve motion. In contrast, although a similar changing trend is shared in (c), a more apparent changing trajectory can be observed. Moreover, more peaks and a wider Doppler spread can also be demonstrated. High dynamic scattering environments can bring a wider range of Doppler frequencies than low dynamic scattering environments. Therefore, a larger Doppler spread and more peaks can be perceived at the same time.

Figure 8 illustrates the delay PSD (a) and angular PSD (b) for curved moving vehicles. It is worth noting that each cluster has a unique survival time as well as BD property in both (a) and (b). In addition, the LoS component contains the strongest power. It can be seen in (a) that as the increase of the delay, the power of MPCs generally decreases. Due to the fact that the movement of vehicles involves a process of approaching and moving away, the delay also shows a smoothly curved trajectory with time. Correspondingly in (b), due to differences in angular velocities of vehicles, the AoD of the LoS component is also shown as an irregular curve trajectory. Furthermore, AoD trajectories of MPCs exhibit large differences, which result from arbitrary motions

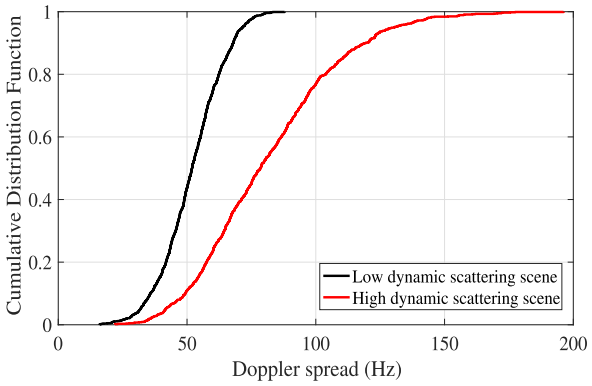

Fig. 9 Doppler spread for different scattering scenarios.

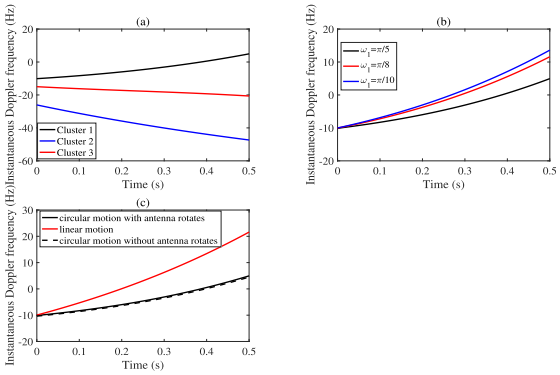

Fig. 10 Instantaneous Doppler frequency.

of clusters. The non-stationarity in angular domain and in delay domain can also be verified simultaneously.

Figure 9 depicts the cumulative distribution function (CDF) of Doppler spreads in different scattering scenes. It can be observed that Doppler spread has a wider distribution in high dynamic scenarios. The reason is that clusters of arbitrary motions have an impact on Doppler frequencies and largely expand the distribution range of Doppler frequencies. As a consequence, a larger Doppler spread leads to a wider Doppler PSD in high dynamic scenarios, verified in Fig. 6.

Then we investigate instantaneous Doppler frequencies in Fig. 10. It can be intuitively seen that due to the differences of cluster motion modes, instantaneous Doppler frequencies have completely different changing trends over time in (a). Shown in (b), as the increase of the angular velocity, the instantaneous Doppler frequency becomes smaller. Due to the direct influence of ω_1 on instantaneous Doppler frequencies, the effect of ω_1 on the time correlation is verified once again. Figure 9(c) shows a large difference in instantaneous Doppler frequencies between linear motion and circular motion. Therefore, different motion modes can contribute to different changing trends of Doppler PSDs and time correlations. Additionally, we can note that despite a slight impact on the instantaneous Doppler frequency, antenna rotates can also contribute to the variation.

Space cross-correlation functions (CCFs) with different time are shown in Fig. 11. It shows that circular motion

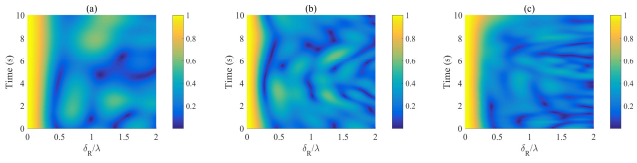

Fig. 11 Space CCF with different time. (a) Linear motion, low dynamic clusters. (b) Circular motion, low dynamic clusters. (c) Circular motion, high dynamic clusters.

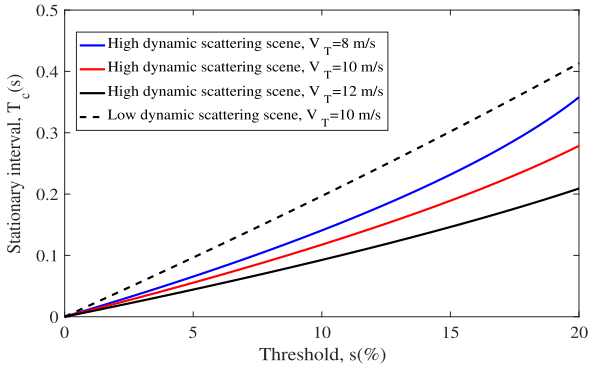

Fig. 12 Quasi-stationary intervals for different scattering scenes and velocities.

brings more significant variations to the space CCF than linear motion with time. Undoubtedly, antenna rotates and changes in vehicle position will affect the angular spread and the space CCF largely. Compared with low dynamic scattering environments, a smaller space CCF can be viewed in high dynamic scattering environments. Patently, random motions of clusters accelerate changes in the channel environment and result in a wider angle spread, which greatly reduces the spatial correlation.

Quasi-stationary intervals with different velocities and for different scattering scenes are shown in Fig. 12. It can be found that as the increase of the velocity, the quasi-stationary intervals are approximately 0.08s, 0.10s, and 0.12s, respectively. It can be concluded that a larger speed will cause a shorter quasi-stationary interval. That's because a larger speed will cause greater changes in channel parameters, which contribute to the high dynamic characteristic of channel environments. Another observation is that low dynamic scattering scenes bring a larger stationary interval. It can be explained that clusters moving with slower speeds can lead to slower variations of channel parameters and induce a slower change in channel environments, which increases the time interval of the wide-sense stationary condition.

6. Conclusion

In this paper, a cluster-based 3D non-stationary V2V channel model with circular arc motions and antenna rotates is proposed. Complex scattering environments are modeled by multiple twin-clusters with arbitrary velocities and directions. A novel cluster evolution algorithm with time-array consistency is developed. The birth, death, and rebirth prop-

erties of clusters are fully taken into consideration for time evolution. For array evolution, the developed VR method is verified to be practical for circular motions. A detailed derivation of ST-CF with circular arc motions is improved. Statistical properties including ST-CF, Doppler PSD, quasi-stationary interval, instantaneous Doppler frequency, RMS-DS, delay PSD, and angular PSD are derived and analyzed. The result shows that as the increase of the transmitting speed, the temporal ACF becomes smaller and the stationary interval also gets smaller. Linear motion and circular motion lead to noticeably different variations of instantaneous Doppler frequency, temporal ACF, Doppler PSD, and spatial CCF with time. The variation of trajectory and the non-stationarity can also be observed in delay PSD and angular PSD. In addition, high dynamic scattering environment would contribute to a smaller temporal ACF, a smaller spatial CCF, and more peaks as well as a wide Doppler spread of Doppler PSD. Moreover, high dynamic scattering environments also result in a short stationary interval. To sum up, we can conclude that the proposed model ensures the non-stationarity in time, space, delay, and angular domains. The motion mode and channel environment both have a significant influence on statistical properties.

References

[1] X. Cheng, Z. Huang, and L. Bai, "Channel nonstationarity and consistency for beyond 5G and 6G: A survey," IEEE Commun. Surveys Tuts., vol.24, no.3, pp.1634–1669, 2022.
[2] J. Liu, Y. Shi, Z.M. Fadlullah, and N. Kato, "Space-air-ground integrated network: A survey," IEEE Commun. Surveys Tuts., vol.20, no.4, pp.2714–2741, 4th Quart., 2018.
[3] O. Elijah, C.Y. Leow, T.A. Rahman, S. Nunoo, and S.Z. Iliya, "A comprehensive survey of pilot contamination in massive MIMO — 5G system," IEEE Commun. Surveys Tuts., vol.18, no.2, pp.905–923, 2016.
[4] A.F. Molisch, Wireless Communications, vol.34, John Wiley and Sons, 2012.
[5] C.-X. Wang, X. Cheng, and D. Laurenson, "Vehicle-to-vehicle channel modeling and measurements: Recent advances and future challenges," IEEE Commun. Mag., vol.47, no.11, pp.96–103, 2009.
[6] X. Zhang, P. Tang, L. Tian, and J. Zhang, "Millimeter-wave channel characteristics for V2V communications in the garage entrance," 2020 14th European Conference on Antennas and Propagation (EuCAP), IEEE, 2020.
[7] H. Wang, J. Rodríguez-Piñeiro, X. Yin, H. Wang, and Z. Yu, "Comparison analysis of 2.4 GHz and mm-wave V2V channel modelling based on measurements," 2019 13th European Conference on Antennas and Propagation (EuCAP), IEEE, 2019.
[8] S. Jiang, X. Zhang, W. Wang, M. Yang, and R. He, "Measurement and diffuse multipath analysis of V2V propagation channel at 5.9 GHz in tunnel area," 2020 14th European Conference on Antennas and Propagation (EuCAP), IEEE, 2020.
[9] D. Czaniera, M. Käske, G. Sommerkorn, C. Schneider, R.S. Thomä, G. Del Galdo, M. Boban, and J. Luo, "Investigation on stationarity of V2V channels in a highway scenario," 2019 13th European Conference on Antennas and Propagation (EuCAP). IEEE, 2019.
[10] S. Jiang, W. Wang, and I. Rashdan, "V2V channel modeling at 5.2 GHz for highway environment," China Commun., vol.19, no.11, pp.112–128, 2022.
[11] M. Yang, B. Ai, R. He, Z. Ma, Z. Zhong, J. Wang, L. Pei, Y. Li, J. Li, and N. Wang, "Non-stationary vehicular channel characterization in complicated scenarios," IEEE Trans. Veh. Technol., vol.70, no.9, pp.8387–8400, 2021.
[12] R. Sun, D.W. Matolak, and P. Liu, "5-GHz V2V channel characteristics for parking garages," IEEE Trans. Veh. Technol., vol.66, no.5, pp.3538–3547, 2016.
[13] M. Hofer, D. Loschenbrand, S. Zelenbaba, A. Dakic, B. Rainer, and T. Zemen, "Wireless 3 GHz and 30 GHz vehicle-to-vehicle measurements in an urban street scenario," 2022 IEEE 96th Vehicular Technology Conference (VTC2022-Fall), IEEE, 2022.
[14] T. Abbas, J. Nuckelt, T. Kurner, T. Zemen, C.F. Mecklenbrauker, and F. Tufvesson, "Simulation and measurement-based vehicle-to-vehicle channel characterization: Accuracy and constraint analysis," IEEE Trans. Antennas Propag., vol.63, no.7, pp.3208–3218, 2015.
[15] J. Nuckelt, T. Abbas, F. Tufvesson, C. Mecklenbrauker, L. Bernado, and T. Kurner, "Comparison of ray tracing and channel-sounder measurements for vehicular communications," 2013 IEEE 77th Vehicular Technology Conference (VTC Spring), IEEE, 2013.
[16] P. Gorniak, "The effective ray-tracing algorithm for analysis of mm-wave V2V propagation channels," 2021 IEEE 93rd Vehicular Technology Conference (VTC2021-Spring), IEEE, 2021.
[17] E. Aksoy, H. Khan, Y. Chen, L. Raschkowski, L. Thiele, and S. Stanczak, "Analysis of varying car geometry accuracies for ray tracing simulations in urban V2V scenarios," 2023 17th European Conference on Antennas and Propagation (EuCAP), IEEE, 2023.
[18] H. Jiang, Y. Xue, J. Zhou, Z. Chen, J. Dang, and L. Wu, "A 3D cylinder MIMO channel model for 5G macrocell mobile-to-mobile communication systems," IEEE Access, vol.7, pp.119350–119356, 2019.
[19] H. Jiang, Z. Chen, J. Zhou, J. Dang, and L. Wu, "A general 3D non-stationary wideband twin-cluster channel model for 5G V2V tunnel communication environments," IEEE Access, vol.7, pp.137744–137751, 2019.
[20] Yi Yuan, C.-X. Wang, Y. He, M.M. Alwakeel, and El-H.M. Aggoune, "3D wideband non-stationary geometry-based stochastic models for non-isotropic MIMO vehicle-to-vehicle channels," IEEE Trans. Wireless Commun., vol.14, no.12, pp.6883–6895, 2015.
[21] Y. Li, X. Cheng, and N. Zhang, "Deterministic and stochastic simulators for non-isotropic V2V-MIMO wideband channels," China Commun., vol.15, no.7, pp.18–29, 2018.
[22] X. Tian, Z. Dou, L. Qi, and Y. Qiu, "A 3D wideband channel model and its statistical properties in V2V scenarios," 2023 8th International Conference on Intelligent Computing and Signal Processing (ICSP), IEEE, 2023.
[23] L. Bai, Z. Huang, H. Du, and X. Cheng, "A 3-D nonstationary wideband V2V GBSM with UPAs for massive MIMO wireless communication systems," IEEE Internet Things J., vol.8, no.24, pp.17622–17638, 2021.
[24] H. Jiang, Z. Zhang, L. Wu, J. Dang, and G. Gui, "A 3-D non-stationary wideband geometry-based channel model for MIMO vehicle-to-vehicle communications in tunnel environments," IEEE Trans. Veh. Technol., vol.68, no.7, pp.6257–6271, 2019.
[25] Jiang, Hao, et al., "A non-stationary geometry-based scattering vehicle-to-vehicle MIMO channel model," IEEE Commun. Lett., vol.22, no.7, pp.1510–1513, 2018.
[26] L. Bai, Z. Huang, Y. Li, and X. Cheng, "A 3D cluster-based channel model for 5G and beyond vehicle-to-vehicle massive MIMO channels," IEEE Trans. Veh. Technol., vol.70, no.9, pp.8401–8414, 2021.
[27] Zhu, Qiuming, et al., "A novel 3D non-stationary vehicle-to-vehicle channel model and its spatial-temporal correlation properties," IEEE Access, vol.6, pp.43633–43643, 2018.
[28] S. Wu, C.-X. Wang, E.-H.M. Aggoune, M.M. Alwakeel, and X. You, "A general 3-D non-stationary 5G wireless channel model," IEEE Trans. Commun., vol.66, no.7, pp.3065–3078, 2017.
[29] Z. Huang, L. Bai, M. Sun, X. Cheng, P.E. Mogensen, and X. Cai, "A mixed-bouncing based non-stationarity and consistency 6G V2V channel model with continuously arbitrary trajectory," IEEE Trans. Wireless Commun., vol.23, no.2, pp.1634–1650, 2024.
[30] Y. Yang, Q. Zhu, W. Li, X. Chen, W. Zhong, X. Yu, and K. Mao, "A

general 3D non-stationary twin-cluster model for vehicle-to-vehicle MIMO channels," 2018 10th International Conference on Wireless Communications and Signal Processing (WCSP), IEEE, 2018.
[31] Q. Zhu, K. Jiang, X. Chen, W. Zhong, and Y. Yang, "A novel 3D non-stationary UAV-MIMO channel model and its statistical properties," China Commun., vol.15, no.12, pp.147–158 2018.
[32] J. Bian, J. Sun, C.-X. Wang, R. Feng, J. Huang, Y. Yang, and M. Zhang, "A WINNER+ based 3-D non-stationary wideband MIMO channel model," IEEE Trans. Wireless Commun., vol.17, no.3, pp.1755–1767 2017.
[33] Y. Li, R. He, S. Lin, K. Guan, D. He, Q. Wang, and Z. Zhong, "Cluster-based nonstationary channel modeling for vehicle-to-vehicle communications," IEEE Antennas Wireless Propag. Lett., vol.16, pp.1419–1422, 2016.
[34] L. Bai, Z. Huang, X. Zhang, and X. Cheng, "A non-stationary 3D model for 6G massive MIMO mmWave UAV channels," IEEE Trans. Wireless Commun., vol.21, no.6, pp.4325–4339, 2021.
[35] Z. Huang, X. Cheng, and X. Yin, "A general 3D non-stationary 6G channel model with time-space consistency," IEEE Trans. Commun., vol.70, no.5, pp.3436–3450, 2022.
[36] Y. Liu, C.-X. Wang, J. Huang, J. Sun, and W. Zhang, "Novel 3-D nonstationary mmWave massive MIMO channel models for 5G high-speed train wireless communications," IEEE Trans. Veh. Technol., vol.68, no.3, pp.2077–2086, 2018.
[37] S. Wu, C.-X. Wang, El-H.M. Aggoune, M.M. Alwakeel, and Y. He, "A non-stationary 3-D wideband twin-cluster model for 5G massive MIMO channels," IEEE J. Sel. Areas Commun., vol.32, no.6, pp.1207–1218, 2014.
[38] Z. Su, C. Li, and W. Chen, "A non-stationary cluster-based channel model for low-altitude unmanned-aerial-vehicle-to-vehicle communications," Drones, vol.7, no.10, p.640, 2023.
[39] J. Bian, C.-X. Wang, Y. Liu, J. Tian, J. Qiao, and X. Zheng, "3D non-stationary wideband UAV-to-ground MIMO channel models based on aeronautic random mobility model," IEEE Trans. Veh. Technol., vol.70, no.11, pp.11154–11168, 2021.
[40] Y. Yuan, C.-X. Wang, X. Cheng, B. Ai, and D.I. Laurenson, "Novel 3D geometry-based stochastic models for non-isotropic MIMO vehicle-to-vehicle channels," IEEE Trans. Wireless Commun., vol.13, no.1, pp.298–309, 2013.
[41] H. Jiang, Z. Zhang, L. Wu, and J. Dang, "A non-stationary geometry-based scattering vehicle-to-vehicle MIMO channel model," IEEE Commun. Lett., vol.22, no.7, pp.1510–1513, 2018.

Zixv Su is now a postgraduate student with Wuhan University of Technology. His main research interest is wireless channel modeling.

Wei Chen received his Ph.D. degree in information and communication engineering from the Huazhong University of Science and Technology, Wuhan, China, in 2005. In 1983, he joined Wuhan University of Technology, Wuhan, China, where he is currently a Professor and Doctoral Supervisor. His current research interests include channel measurement and modeling, massive MIMO technology, millimeter wave technology, satellite navigation system theory and technology application, and intelligent traffic control systems.

Yuanyuan Yang received the Ph.D. degree in information and communication engineering from Wuhan University of Technology in 2022. Currently, she is a teacher of School of Information Engineering, Wuhan University of Technology, China. Her research interests include communication signal processing and application, image processing, compressed sensing, and remote sensing.